IET Renewable Power Generation

Research Article

IET Journals
The Institution of Engineering and Technology

Power oscillation damping with virtual capacitance support from modular multilevel converters

ISSN 1752-1416
Received on 29th April 2019
Revised 15th July 2019
Accepted on 2nd August 2019
doi: 10.1049/iet-rpg.2019.0517
www.ietdl.org

Abel A. Taffese[1] ✉, Atsede G. Endegnanew[2], Salvatore D'Arco[2], Elisabetta Tedeschi[1]

[1]*Department of Electric Power Engineering, Norwegian University of Science and Technology, Trondheim, Norway*
[2]*Department of Energy Systems, SINTEF Energy Research, Trondheim, Norway*
✉ *E-mail: abel.taffese@ntnu.no*

Abstract: Power oscillation damping (POD) is one of the ancillary services expected from high-voltage direct current (HVDC) converters. When providing POD to the ac side, converters draw power from the dc side, which can cause distortion to the dc voltage especially in the case of limited dc capacitance. In meshed/multi-terminal HVDC grids, where dc voltage regulation is distributed using a dc voltage droop control strategy, the distortion due to the POD controller action is propagated to other connected ac grids because of the droop action. This propagation can be reduced by using the inherent energy storage capability of the modular multilevel converter (MMC), which is a common converter topology for HVDC. Different methods to utilise the energy stored in the MMC for the purpose of POD have been proposed in the literature. This study presents a detailed analysis and experimental validation of one of these methods, referred to as virtual capacitance support, which increases the effective dc grid capacitance by using the stored energy of multiple MMCs connected in the same grid. The experiments, which were carried out using power hardware in the loop setup, demonstrated the effectiveness of the method.

1 Introduction

Massive integration of remote renewable energy sources and the need for flexible power trading between neighbouring countries have led to the installation of numerous high-voltage direct current (HVDC) interconnectors. Due to the increased presence of HVDC converters, transmission system operators are requiring them to have the capability to provide services such as power oscillation damping (POD) to connected ac networks, which were traditionally delivered by equipment like synchronous generators [1]. A number of studies on POD using power electronic converters can be found in recent literature [2–7]. The main goal of a POD controller is to improve damping of electromechanical modes (usually in the range 0.2–2 Hz [8]) by modulating either active or reactive power [3]. This paper focuses on POD using the former approach where the converter injects active power into the ac side at the frequency of the oscillation but in counter phase. The challenge of using active power is that it has to be balanced instantaneously by power drawn from another source. In traditional POD implementations using HVDC converters, this other power source is the dc link (grid) capacitance, which has a very limited storage capacity. Consequently, the dc voltage can be distorted by the oscillation, which can be particularly challenging in meshed/multi-terminal dc grids where dc voltage regulation is often distributed by using the droop method. This is because converters participating in the dc voltage regulation react to the voltage distortion by injecting an opposing active power drawn from their respective ac grids. This effectively couples the ac networks and leads to the propagation of the low-frequency oscillations between the ac grids. In addition to the disturbance experienced by the other ac grids, the propagation of the oscillations also indicates that there can be an inter-ac-grid dynamic coupling in the electromechanical range. This can lead to undesired interaction between power system stabilisers located in different ac grids, such as the one reported in [9]. This problem can be mitigated by leveraging the energy storage capability of the modular multilevel converter (MMC), which is currently the most flexible and preferred converter topology for HVDC. The MMC is composed of strings of sub-modules, each with its own capacitors that are suited for quickly absorbing and releasing fluctuating active power in the electromechanical range.

Two approaches for utilising the MMC energy in such a manner are found in literature [10–12]: (i) cancelling the oscillation in the dc side by injecting the required power from the capacitors of the source converter (the one providing POD) [10, 11] and (ii) increasing the apparent capacitance of the dc grid by emulating a large capacitance using the energy stored across multiple MMC [12]. A limitation of the first approach is that the amount of power that can be buffered by the arm capacitors is limited, especially at lower frequencies (e.g. 0.2 Hz). The second method overcomes this by distributing responsibility among multiple converters connected to the same dc grid [12]. Each converter needs only a local measurement of dc voltage to emulate a virtual capacitance. This virtual capacitance can be an order of magnitude (or more) larger than the equivalent dc grid capacitance. Since this capacitance appears in parallel to the dc grid capacitance, it provides a low impedance path for current (and hence, power) at the oscillation frequency. This method will be referred to as virtual capacitance support (VCS) henceforth. VCS can offer functionality that would otherwise require a dedicated converter connected to energy storage, which would be more expensive and bulkier. This makes the VSC attractive because it can be implemented by adding a few extra sub-modules or by increasing the capacitance and operating voltage of the sub-modules. This will be discussed further later in this paper. An additional benefit of VSC is that it can improve transient stability of the dc grid since the apparent grid capacitance is increased. This can be compared with virtual inertia support in ac grids [13]. Other methods for emulating virtual capacitance using the energy storage of the MMC can be found in literature [14–16]. However, as will be shown later, these methods are not suitable for emulating the large capacitance value required by VCS.

An initial formulation of the VCS method, together with a preliminary analysis, was presented in [12]. The analysis in [12] represents the ac grids by ideal voltage sources with the POD controller effect emulated by an oscillating active power injection. This can be used to show the basic principle of the method. However, the results in [12] are not sufficient to show the feasibility of the method under practical conditions. This paper presents extensive analysis and validation of the VCS method using modal analysis and time-domain simulations under more realistic conditions. Unlike [12], this paper uses a multi-machine system with a proper representation of the POD effects. Moreover, the method is experimentally validated on an 18-level MMC using a power hardware in the loop (PHIL) approach, which is a

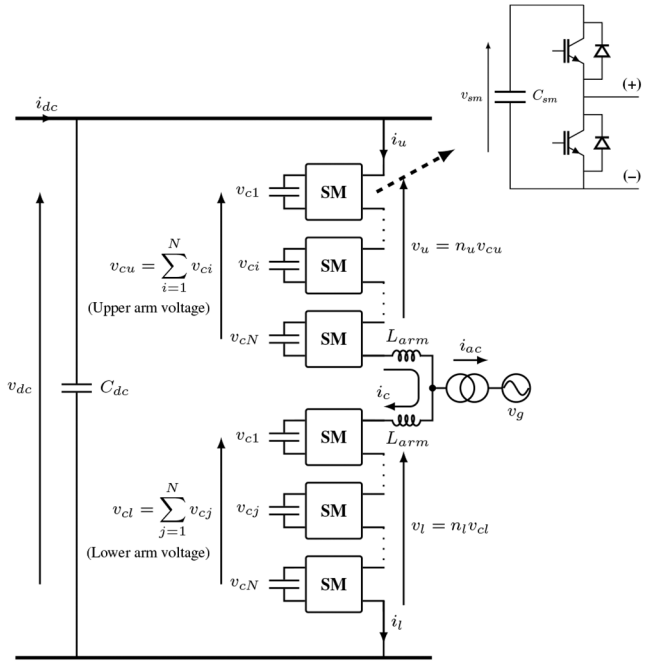

Fig. 1 *Per-phase circuit of the MMC*

technique for testing power equipment under realistic grid conditions [17, 18].

The remainder of this paper is organised as follows. An average model of the MMC is presented in Section 2, followed by a description of the VCS method in Section 3. The case study system is introduced and analysed in Section 4. The analysis focuses on identifying poorly damped inter-area modes in the system. Section 5 discusses the design of a POD controller to damp the identified inter-area mode. The results are presented in Sections 6 and 7.1 followed by discussion and conclusions in Sections 8 and 9, respectively.

2 Modelling of the MMC

A simplified average model of the MMC suitable for representing power balance and energy dynamics is presented in this section. Dynamics of the MMC is affected by the adopted modulation technique, which is the method for calculating the insertion indexes from the voltage references. The method used in this paper is compensated modulation (CM) [19], also known as indirect modulation [20], which calculates the insertion indexes by dividing the voltage reference by the respective arm voltages. When CM is used, the ripples in the arm voltages can be neglected without affecting the accuracy of the model [21]. This means that the MMC energy can be represented by one aggregate state if the average values of the arm voltages are assumed to be balanced [21]. Thus, only one arm energy state is used per MMC. All the equations in this section are in per-unit with the base values specified in the Appendix. The base value for the energy [W_b in (13) in the Appendix] is chosen so that the relation between arm voltage and arm energy is given by

$$w = v^2 \tag{1}$$

where w and v are the arm energy and the arm voltage, respectively, in per-unit. Fig. 1 shows one leg of a three-phase MMC, together with the definition of important variables and their respective polarities. The analysis in this work is not strictly dependent on the type of sub-module, which means that the results are applicable to different sub-module topologies. However, for the sake of clarity half-bridge sub-modules are assumed in the following (see Fig. 1) because the half-bridge topology in general offers fewer features than a full-bridge topology. For the purpose of the derivation, the upper and lower arm inserted voltages, v_u and v_l, are decomposed into common-mode, v_c, and differential, v_{ac}, components as given by

$$\begin{aligned} v_c &= \frac{1}{2}(v_u + v_l) \\ v_{ac} &= (-v_u + v_l) \end{aligned} \tag{2}$$

The arm current is also similarly decomposed as shown in

$$\begin{aligned} i_c &= \frac{1}{2}(i_u + i_l) \\ i_{ac} &= \frac{3}{4}(i_u - i_l) \end{aligned} \tag{3}$$

The scaling factors result from the per-unit conversion where the arm voltages and currents are divided by the dc base values, while the ac quantities are divided by the ac base values. The average energy dynamics of the MMC shown in (4) can be derived by using these definitions of ac and common mode quantities:

$$\begin{aligned} \frac{\mathrm{d}}{\mathrm{d}t}w &= \frac{2}{c_p}\left[\frac{1}{2}(v_{dc}^* - 2v_c^*)i_c - \frac{1}{6}v_{dq}^* \cdot i_{dq}\right] \\ &= \frac{1}{3}\frac{1}{c_p}(p_{dc} - p_{ac}) \end{aligned} \tag{4}$$

where c_p is the per-unit arm equivalent capacitance, and i_c is the circulating (common-mode) current. v_{dq}^* and i_{dq} are the ac voltage reference and the ac current in dq domain, respectively. Equation (4) shows that the stored energy is constant when the ac and dc powers of the converter are balanced. The dynamics of i_c and v_{dc} are shown in (5) and (6), respectively:

$$\frac{\mathrm{d}}{\mathrm{d}t}i_c = \frac{1}{l_{dc}}(v_c^* - r_{dc}i_c) \tag{5}$$

where l_{dc} and r_{dc} are the arm inductance and resistance in per-unit to the dc base values:

$$\frac{\mathrm{d}}{\mathrm{d}t}v_{dc} = \frac{1}{c_{dc}}(i_{dc} - 3i_c) \tag{6}$$

where i_{dc} is the dc line current and c_{dc} is the equivalent dc side capacitance in per-unit. The ac current dynamics are given by

$$\begin{aligned} \frac{\mathrm{d}}{\mathrm{d}t}i_{dq} &= \frac{1}{l_{ac}}(v_{dq}^* - v_{gdq} - r_{ac}\boldsymbol{I} \cdot i_{dq} - \omega l_{ac}\boldsymbol{J} \cdot i_{dq}) \\ \boldsymbol{I} &= \begin{bmatrix} 1 & 0 \\ 0 & 1 \end{bmatrix} \quad \text{and} \quad \boldsymbol{J} = \begin{bmatrix} 0 & -1 \\ 1 & 0 \end{bmatrix} \end{aligned} \tag{7}$$

where ω is the fundamental frequency in rad/s and v_{gdq} is the grid voltage in the dq domain. The variables l_{ac} and r_{ac} are the equivalent ac side inductance and resistance in per-unit to the ac base values. Equations (4)–(7) constitute a fifth-order model [21] used to represent the MMC in this paper.

3 Virtual capacitance support

The power balance in the MMC can be achieved using arm energy controllers, which are implemented using cascaded PI [12]. Under normal operation, the reference to the energy controller, w^*, is set to a constant value. This means that the controller tries to balance any change in ac power with power from the dc side so that the arm energy stays constant. In the case where the MMC is involved in POD, oscillating active power (0.2–2 Hz [8]) needs to be injected into the ac side. The energy controller transfers the oscillation to the dc side, which is then propagated further into other connected ac grids interfaced by converters participating in dc voltage regulation. This can be avoided if the energy controller is designed not to balance the oscillating part of the ac power into the dc side, and instead diverts the oscillation from the dc side to

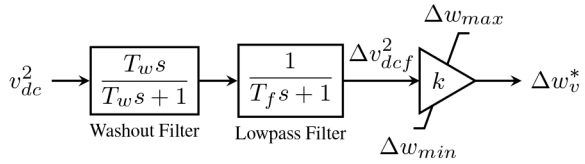

Fig. 2 *Block diagram of the VCS scheme [12]*

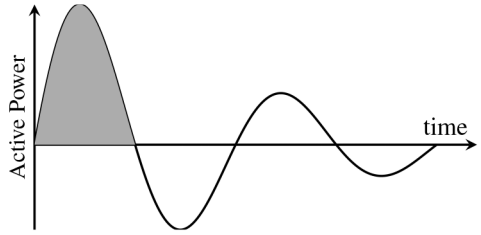

Fig. 3 *Active power injected during POD. The maximum energy deviation is the area under the largest swing*

the arm capacitors. This is achieved in this paper by adopting the VCS method, which emulates a virtual capacitance using the MMC energy storage by generating the energy reference from the dc voltage measurement as shown in (8) [14, 15]:

$$w_v^* = k_v \frac{\mathrm{d}}{\mathrm{dt}} v_{\mathrm{dc}}^2 \tag{8}$$

where w_v^* is the virtual energy reference and k_v the virtual capacitance normalised by the arm capacitance. For example, $k_v = 1$ gives a virtual capacitance equal to the six times the arm capacitance of the MMC (one per arm). The corresponding arm voltage when providing VCS using (8) is given by

$$v_v = \sqrt{k_v} v_{\mathrm{dc}} \tag{9}$$

The arm voltage is normally designed to be close to the dc voltage to minimise size and cost of the converter. This implies that the value of k_v has to be close to one to give a feasible solution. However, it was concluded in [12] that the value of k_v should be in the order of 100 to give sufficient virtual capacitance for the purpose of diverting the POD oscillation. Therefore, the method given by (8) is not suitable for the application in this paper. Shinoda *et al*. [16] propose a method which subtracts the nominal dc energy from the energy reference as shown in

$$w_v^* = k_v\left(v_{\mathrm{dc}}^2 - v_{\mathrm{dc0}}^2\right) \tag{10}$$

where v_{dc0} is the nominal dc voltage. This approach decouples the nominal dc voltage from the emulated capacitance, which enables larger values of k_v compared to (9). However, slow changing deviations around the nominal voltage can cause large energy changes. For example a 1% variation of the dc voltage with $k_v = 100$ results in a 2 pu change in energy, which is not practical. Therefore, this paper uses a modified capacitance emulation scheme [12] that acts on the changes in dc voltage Δv_{dc}, which does not contain dc or slowly varying components.

A block diagram of the VCS scheme is shown in Fig. 2, where the washout filter is used to remove the dc (constant) component and slow changes in the dc voltage (i.e. extract Δv_{dc}^2 from v_{dc}^2), and the low-pass filter reduces the gain at high frequencies to avoid noise amplification and instability problems. The output, Δw_v^*, is added to the constant energy reference, w^*. The filter time constants are chosen such that there is a close to zero phase shift around the frequency of interest (0.2–2 Hz) in order to satisfy the relation between dc voltage and energy given in (8) around the oscillation frequency. Lead-lag filters can be used if additional phase adjustment is needed, for instance, to compensate for the lag introduced by the energy controller. The upper limit $\Delta w_{\max}$ in Fig. 2 is placed to avoid exceeding the voltage rating of the arms (the sub-modules), while the lower limit, $\Delta w_{\min}$, is used to avoid over-modulation. Over-modulation occurs when the arm voltage is below the reference for the inserted voltage. This results in saturation of the insertion indexes, which leads to loss of control, and generation of harmonics [22].

3.1 Energy storage requirements

The implementation of the VCS method places a constraint on the arm voltage operating point because it is desired to provide the service without disrupting the normal operation of the converter by causing over-modulation. In order to avoid over-modulation, the converter should be run with the arm voltage being higher than the maximum inserted voltage reference. This gives headroom for downward changes in the arm voltage without over-modulation. The size of the headroom defines the amount of energy available for the service without affecting normal operation of the converter. The maximum deviation in energy, $\Delta\hat{w}_{\max}$, for a given peak POD power output by the converter, $\hat{p}$, is calculated by computing the area under the largest active power swing (see Fig. 3) as given in (11) [11], which is derived by neglecting the effect of damping over one swing:

$$\Delta\hat{w}_{\max} = \frac{1}{6}\frac{1}{M}\frac{2}{c_{\mathrm{p}}}\frac{2\hat{p}}{\omega_{\mathrm{osc}}} \tag{11}$$

where c_{p} is the per-unit arm capacitance, M is the number of converters providing VCS, and ω_{osc} is the oscillation frequency in rad/s. The factor 1/6 is because the ac active power is shared equally among the six arms. In (11), it is assumed that all the converters are contributing to the VCS equally. The corresponding maximum arm voltage deviation, $\Delta\hat{v}_{\max}$, can be calculated from the relationship between arm energy and voltage [see (11)]:

$$\Delta\hat{w}_{\max} = \Delta\hat{v}_{\max}^2 + 2V_0\Delta\hat{v}_{\max} \tag{12}$$

where V_0 is the nominal dc arm voltage in per-unit. The maximum arm energy variation is inversely proportional to the frequency of oscillation, which means that for the same maximum energy variation, more POD power can be absorbed at higher frequencies. For example, a 900 MW converter with an arm capacitance of 0.015 pu can absorb up to 25 MW peak power at 1 Hz and 12.5 MW at 0.5 Hz for the same maximum energy deviation of 0.2 pu. More detailed analysis of the energy storage requirement and its sensitivity to frequency and other system parameters are presented in [11]. It should be noted that for the case of POD, the two limits in Fig. 2 should be chosen to accommodate the largest power swing. This is because in the worst case of zero damping the power oscillation will have equal positive and negative peaks.

From (11) and (12), it can be concluded that the arm voltage should have a headroom of at least $\Delta\hat{v}_{\max}$ above the maximum inserted voltage (i.e. the rated dc link voltage). Such a headroom can be obtained in two ways [11]: (i) increasing the number of sub-modules, and (ii) increasing the voltage rating of each sub-module so that the arm can be operated at a higher voltage. Additionally, the arm capacitance can be increased to reduce $\Delta\hat{v}_{\max}$. Option (i) is promising for existing designs because the MMC normally has extra sub-modules for the purpose of redundancy, which can be leveraged for this purpose. However, for new designs, a better solution can be found by optimising, for cost and volume, a combination of the two options and an increase in the arm capacitance.

4 Case study system

The system used for the case studies in this paper is shown in Fig. 4. It is composed of three isolated ac grids that are interconnected by a three terminal MMC-based MTDC network. Two of the ac grids are onshore ac networks (AC Grid 1 and 2), while the third ac grid is an offshore wind-farm represented by a single equivalent generator, G4. AC Grid 2 has two areas that are 110 km apart: Area 1 with G2 and G3, and Area 2 with G5.

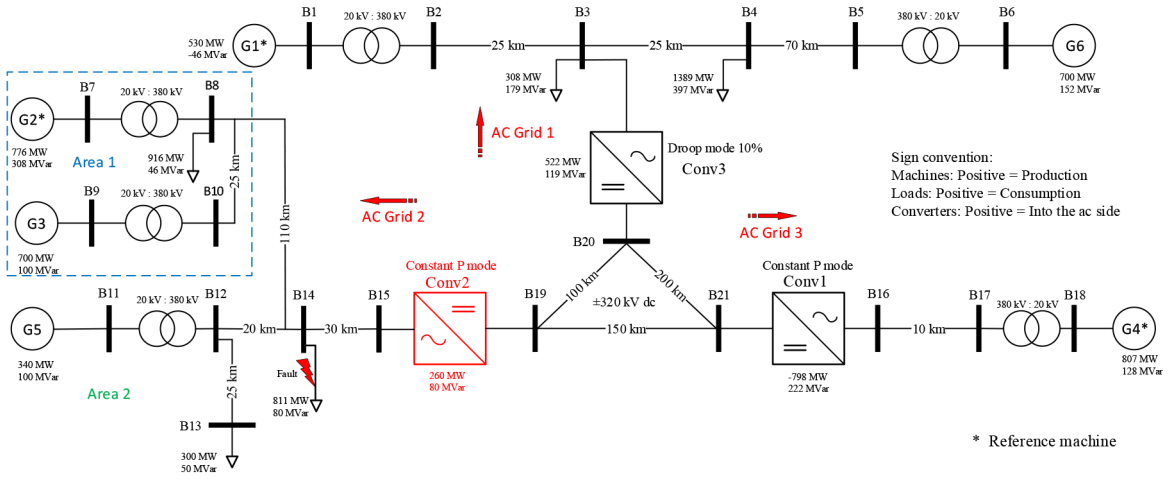

Fig. 4 *Case study system*

Table 1 Poorly damped electromechanical modes

No.	Mode	Damping, %	Frequency, Hz
1	−0.1948 + 5.8377i	3.34	0.93
2	−0.0814 + 3.3027i	2.46	0.525

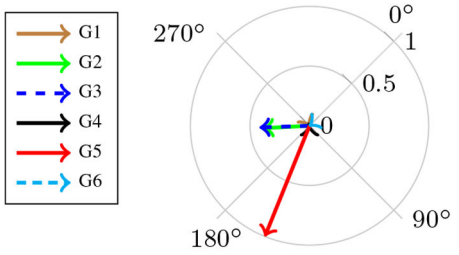

Fig. 5 *Observability of Mode 2 in rotor speed states of the generators*

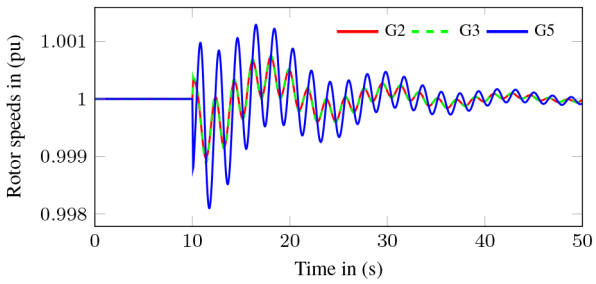

Fig. 6 *Rotor speed of generators in AC Grid 2*

The model of the case study system was built using custom library components developed using Simscape Language from MathWorks [23]. All component models are in *dq* domain with constant values in the steady state so that it is possible to use the same model for linear analysis. The generators are represented using a detailed sixth-order machine models and were validated against DigSilent PowerFactory [24]. The MMC is represented by a simplified fifth-order model presented in Section 2. All converters are equipped with active and reactive power controller. Conv1 is controlled in droop mode, while Conv2 and Conv3 are controlled in constant power mode. Conv2 (shown in red in Fig. 4) is replaced by a physical converter for PHIL testing as explained in Section 7.1. Component parameters for the test system, adopted from literature [8, 25], are given in the Appendix. The case study system will be analysed in this section using modal analysis and time-domain simulations in order to identify poorly damped electromechanical modes that will be damped using POD on one of the MMC converters in the MTDC grid.

4.1 Modal analysis

The case study system has 138 states that are associated with the generators, converters, controllers, and measurement filters. The system is linearised around an operating point shown by the load-flow condition depicted in Fig. 4. A definition of *observability* is presented here because it is used frequently in this paper.

Observability measures (or mode shapes): Observability measures are elements of the right eigenvector of the state matrix. They indicate the relative observability of a certain mode in all the states when that mode is excited. The values are complex numbers, where the magnitude shows the extent of the observability and the angle shows the relative phase shift in the states with respect to the mode [8, p. 714].

Two poorly damped electromechanical modes, listed in Table 1, are identified in the study system using the modal analysis. Poorly damped electromechanical modes are defined in this work to have damping below 5% and frequency in the range 0.2–2 Hz. From the observability/mode shapes of speed state variables, Mode 1 is found to be a local mode between G2 and G3. On the other hand, Mode 2 is an inter-area mode with G2 and G3 oscillating together and G5 on the other side is shown in Fig. 5. The inter-area mode, Mode 2, is chosen for further analysis to study the performance of POD with VCS.

4.2 Time-domain analysis

The time-domain simulation results shown in Fig. 6 support the modal analysis presented in the previous section. A fault at bus B14 creates a disturbance in the system and excites the inter-area mode (Mode 2). It can be seen from the generator speeds that an oscillation at ∼0.53 Hz is visible in the response plots. This frequency is the same as the damped natural frequency of Mode 2 in Table 1. The damping is also consistent with the modal analysis result. It can also be observed that G2 and G3 oscillate together while the oscillation in G5 is shifted by ∼ 60° with respect to the other generators. This is an indication of an inter-area mode since G2 and G3 are in Area 1, and G5 is in Area 2.

5 Power oscillation damping

This section presents the design of a POD controller integrated with control of Conv2 to improve the damping ratio of Mode 2 to be above 5%. The input–output pairing for the POD controller is chosen so that the input gives high observability and the output gives high controllability of the selected mode [26]. Using this approach, the input is chosen to be the phase locked loop (PLL) angle (θ_{PLL}) while the output is active power (Δp).

The basic structure of the controllers is shown in Fig. 7. It includes a washout filter, a lead-lag compensation, and a gain with the limiter. The washout filter removes any dc offset from θ_{PLL}, and the lead-lag block provides phase angle adjustment. There can be multiple lead-lag blocks in series depending on the amount of

angle compensation needed. The design of the POD controller parameters is done using the root-locus method [27].

First, root-locus plots are made for the system with active power reference as input and the output of the washout filter as output. Then, the departure angle of the mode of interest is calculated from the plot. The required compensation angle is computed to be the amount of angle required to rotate the departure angle towards 180° so that the maximum possible damping improvement for a given gain is obtained. The gain is chosen to achieve the desired level of damping. For the case study system, the washout filter time constant is chosen to be 5 s, the mode of interest has frequency of 0.53 Hz, and the desired level of damping is >5%. Taking these values into consideration, the resulting design is to have two stages of lead-lag each one providing 48° angle boost, and the gain is set to be $k_{\text{pod}} = -0.06$. Another possibility to achieve the same effect on Mode 2 is to use a positive gain and two lead-lag blocks each providing −42°. However, these values are not adopted because, for this particular case, they cause other modes to be unstable. As one of the goal of the paper is the experimental validation of the VCS method with POD, it should be noted that there is a difference between the simulation and the experimental setup representation of the angles. Since the simulation is in *dq* domain, every angle is measured with respect to the reference machine, which results in constant angle values in the steady state. However, this is not true in practical systems which are in *abc* domain since there is no reference machine and all the angles are linear functions of time and fundamental frequency. Therefore, a washout filter is not sufficient to remove the linear time variation. After passing through the washout, the PLL angle still has a dc offset equal to $\bar{\omega}T_w$, where $\bar{\omega}$ is the steady-state grid frequency. The solution used in this work is to subtract $\bar{\omega}T_w$ from the output of the washout filter (Fig. 7). $\bar{\omega}$ can be calculated by applying filtering or averaging to the PLL frequency over a few tens of seconds so that the electromechanical range is not affected. It should be noted that this subtraction of $\bar{\omega}T_w$ is not necessary for the phasor simulation.

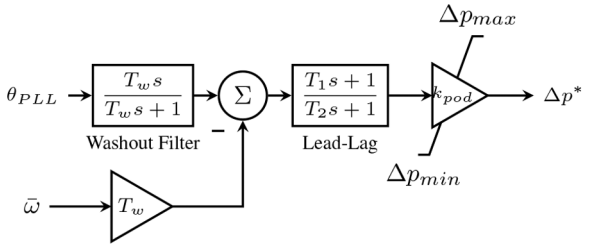

Fig. 7 *POD controller*

Table 2 Mode 2 under different case studies

Case	Mode	Damping, %	Frequency, Hz
base	−0.0814 + 3.30i	2.46	0.525
POD	−0.225 + 3.34i	6.76	0.53
POD + VCS	−0.225 + 3.34i	6.76	0.53

6 Simulation results

This section presents the performance of the VCS method. To this end, three case studies are considered. The first case is a base case where both the POD and VCS are disabled. In the second case, the POD controller is enabled to improve the damping of Mode 2, while in the last case both the POD and VCS controllers are enabled. These three cases are labelled Base, POD, and POD + VCS, respectively. Each case is studied using modal analysis, time-domain simulations, and laboratory experiments. The arm voltages of all the MMCs including the physical one are set to be 10% above the nominal dc voltage. As will be shown, this 10% headroom is more than what is required for VCS. The VCS gain is set to have a value $k_v = 125$.

6.1 Modal results

The values of Mode 2 under the three case studies are shown in Table 2. It can be seen that the POD controller moves the mode to the left with only a minor shift in the frequency, which results in the maximum possible damping improvement for the given gain. Note that the VCS does not affect the location of the mode in the complex plane (Table 2).

Observability of Mode 2 in the speed states of the generators in the system is shown in Table 3. The magnitudes are normalised by the maximum values in each column and presented as percentages. Mode 2 is most observable from the states of G5 as can be seen from the speed in Table 3 and the rotor angles in Table 4. As discussed in Section 4, the mode is an inter-area mode in Grid 2, where G2 and G3 oscillate against G5. This is evident from the observability angles in Table 3. It can be noted that the mode is slightly observable in Grid 1 (0.4% in G1, and 0.6% in G6, for the rotor speeds) even in the base case. This is because the oscillation in the grid appears as a disturbance to the active power controller, which tries to reject it. However, complete rejection of disturbance using a PI controller is only possible at dc. This creates a residual oscillation in active power which is transferred to the dc side by the energy controller. This is then picked-up by converters participating in dc voltage regulation. Converters controlled in constant power mode, such as Conv3, do not pass this oscillation into their ac sides [28]. When POD is enabled the mode becomes more observable in the AC Grid 1 (see G1 and G6 in Table 3). The observability in the speed of G1 increased from 0.4 to 7.6%, and from 0.6 to 9.5% for G6. The same pattern can be observed from Table 4, where the observability of Mode 2 in the rotor angles of G6 increased from 0.8 to 13%. This is in accordance with the

Table 3 Normalised observability of Mode 2 in rotor speeds

Element	Base		POD		POD + VCS	
	Mag, %	Angle, deg	Mag, %	Angle, deg	Mag, %	Angle, deg
G1	0.4	106	7.6	101	1.9	122
G2	38.6	222	37.5	125	37.5	198
G3	41.5	223	40.4	126	40.4	199
G4	0	110	0	112	0	196
G5	100	157	100	65	100	138
G6	0.6	190	9.5	183	2.4	204

Table 4 Normalised observability of Mode 2 in rotor angles

Element	Base		POD		POD + VCS	
	Mag, %	Angle, deg	Mag, %	Angle, deg	Mag, %	Angle, deg
G3	3.2	145	3.4	49	3.4	122
G5	100	42	100	310	100	23
G6	0.8	135	13	131	3.3	152

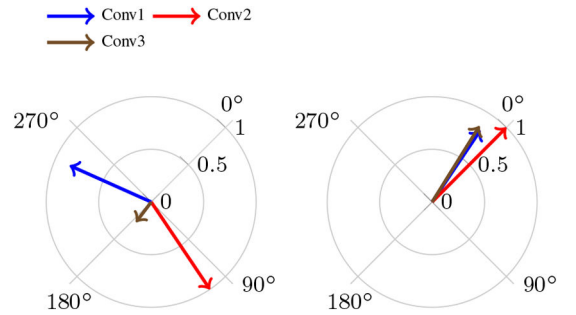

Fig. 8 *Observability of Mode 2 in converter energy states: POD case (left) and POD + VCS case (right)*

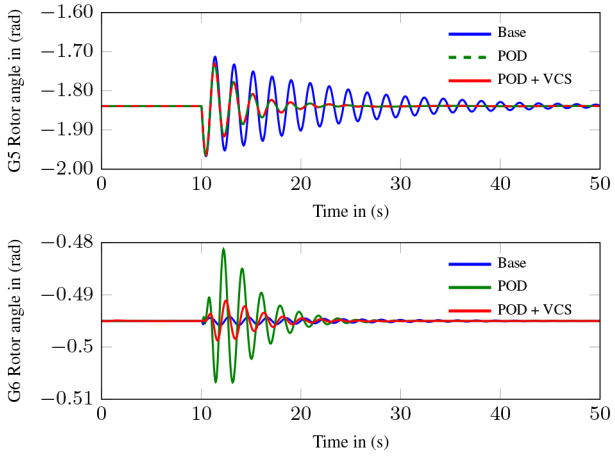

Fig. 9 *Rotor angles of G5 and G6 (simulation)*

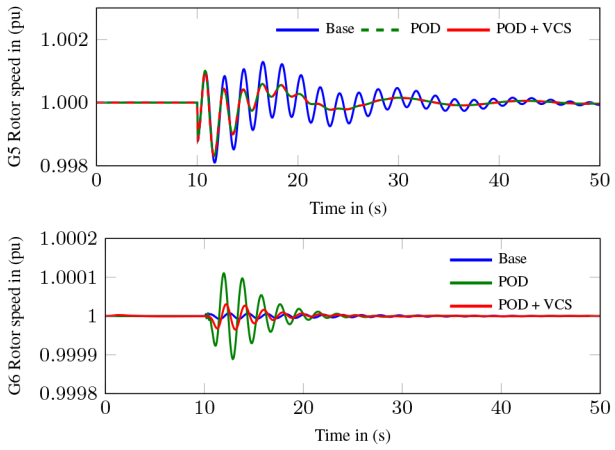

Fig. 10 *Rotor speeds of G5 and G6 (simulation)*

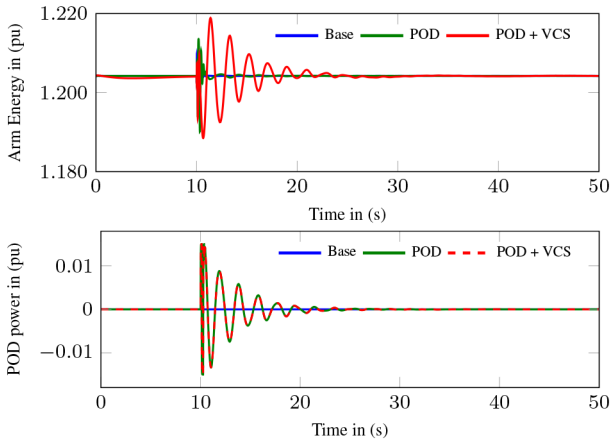

Fig. 11 *Active power and energy measurements of Conv2 (simulation)*

discussion in this paper that POD propagates the oscillation to other connected grids via the dc grid.

When VCS is enabled, the observability of Mode 2 in AC Grid 1 decreased by a factor of more than 3 (Table 3). The same can be seen from the rotor angle in Table 4. Another interesting plot is the observability mode phasor plot of Mode 2 in the MMC energy states of the three converters in Fig. 8. The figure compares the POD case with the POD + VCS case to highlight the changes when the support function is enabled. In the POD case the three energy states are oscillating in different directions (with different phase shifts). In this case the energy controllers are working to keep the MMC energy states constant irrespective of disturbances. They cannot completely reject the oscillations in power because they have a PI structure. Therefore, there is a residual oscillation in the energy states. The phase angle of the observability in Conv2 is close to 90° because there is an integral relationship between active power and energy. For Conv1, the disturbance comes from the dc voltage droop controller, which tries to oppose the oscillating power injected by Conv2. Hence, the observability of Mode 2 in Conv1 energy appears almost opposite to that of Conv2. Since Conv3 is not participating in dc voltage control, observability of the mode in energy state of Conv3 is significantly lower than the others. When VCS is enabled, the three energy states are more aligned with each other and also with the mode (i.e. the observability angles are close to 0°), which means that they are collaborating effectively in absorbing the oscillation. This will be more evident from time-domain results in the next sections.

6.2 Time-domain simulation

Simulation studies were performed based on the three case studies used in this paper. A fault at bus 14, which is applied at 10 s and cleared after 75 ms, is used to excite the inter-area mode in AC Grid 2. The fault is cleared without changing the grid topology, which means that the system dynamic properties before and after the fault are the same. Fig. 9 shows rotor angles of G5 (AC Grid 2) and G6 (AC Grid 1) under the three case studies. The rotor angle of G5 shows that the POD improves the damping of Mode 2. Moreover, by looking at the same figure, it can be noted that there is no visible difference in the damping and frequency of Mode 2 when energy support is enabled, which is in line with the modal analysis results. The same effect can be seen from the rotor speed of G5 in Fig. 10. By looking at the measurements from G6, it can be noted that the machine starts oscillating when POD is activated. The frequency and damping of the oscillation are the same as that of Mode 2 in Table 2. Once VCS is enabled, the oscillation in AC Grid 1 shows a significant reduction (by a factor of 3.4 taking the peak-to-peak ratio). Fig. 11 shows that the energy states start oscillating when VCS is enabled. This confirms that the oscillation is being diverted into the arm capacitors. The variations in arm energy are proportional to the variations in active power when VCS is enabled. This confirms that the oscillation is being diverted into the arm capacitors. The variations in arm energy are proportional to the variations in active power when VCS is enabled.

7 Experimental results

This section presents the experimental results using a PHIL approach. The test cases are the same as those used in the simulation results. A description of the PHIL setup is presented first, followed by the experimental results.

7.1 PHIL setup

The purpose of PHIL in this work is to validate the VCS and POD control schemes on a physical converter under realistic conditions. In the setup, Conv2, a 900 MW converter, is replaced by a scaled down 60 kVA, 18-level MMC. The scaling is such that the per-unit power, voltages, and currents are the same between the simulation and the physical system. This is achieved by exchanging per-unit currents and voltages between the two systems. Fig. 12 shows the test setup including a real-time simulator (from OPAL-RT [29]), a power amplifier (from EGSTON Power [30]), and the MMC (built by SINTEF Energy Research [31]). The simulator is responsible

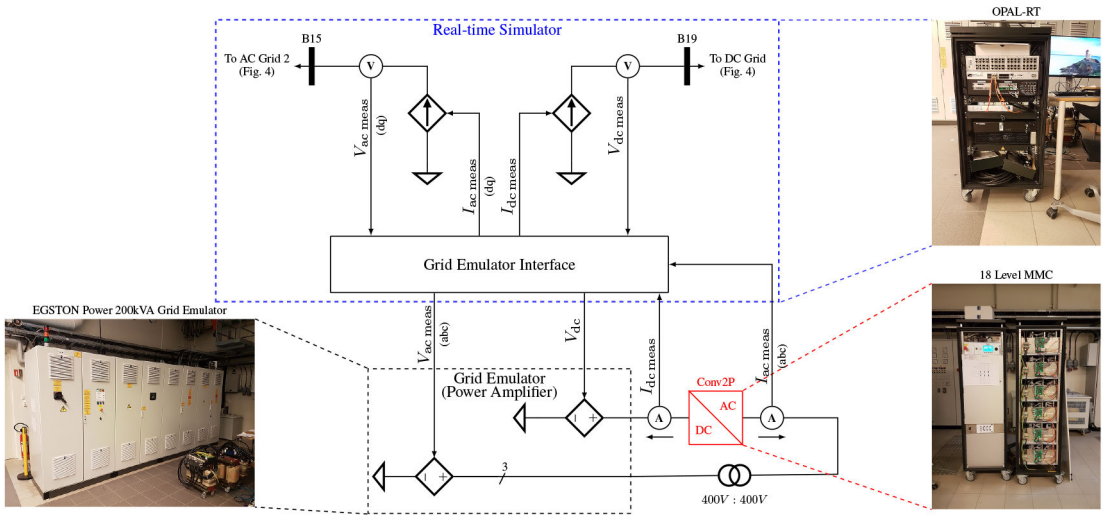

Fig. 12 *PHIL setup*

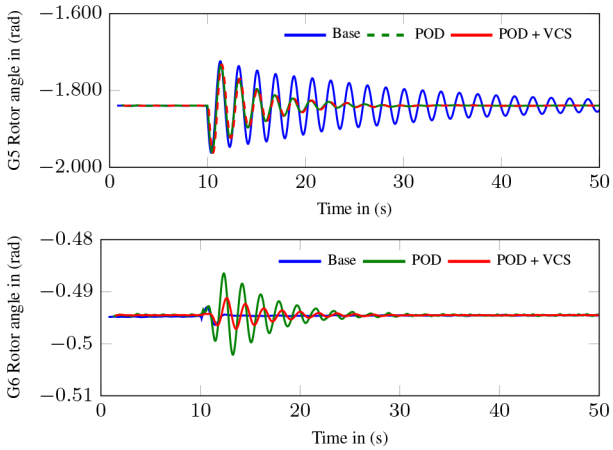

Fig. 13 *Rotor angles of G5 and G6 (experimental)*

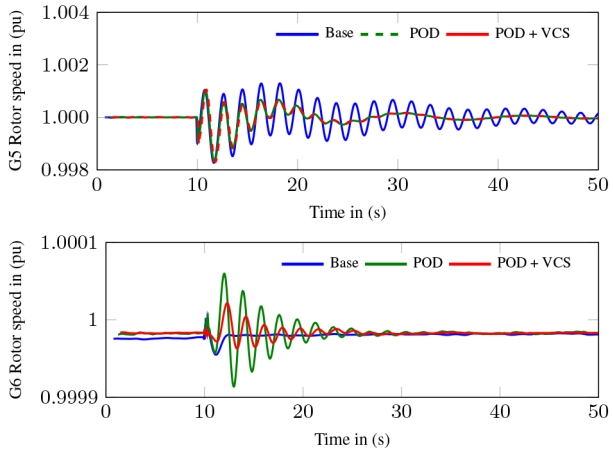

Fig. 14 *Rotor speeds of G5 and G6 (experimental)*

for running the simulated system and interfacing with the power amplifier. The interface is where the scaling and transformations between *abc* and *dq* domain are performed. The transformation is necessary because the ac system is modelled in *dq* domain in the simulation. The principle is that the converter is represented by current injection in the simulation, while the grid is replaced by a controlled voltage source (grid emulator) connected to the actual converter. This arrangement for interfacing the power equipment to a simulated system is known as ideal transformer model [32]. The references to the controlled current sources are obtained from physical current measurements (I_{acmeas} and I_{dcmeas} in Fig. 12). Similarly, the references to the grid emulator come from voltage measurements in the simulation (V_{acmeas} and V_{dcmeas} in Fig. 12). This creates a virtual connection between the physical converter and the simulated system.

7.2 PHIL results

The experiments were conducted at 450 V dc, which is 75% of the base voltage of Conv2P (600 V). Hence, the voltages are scaled such that a 1 pu voltage in simulation results in a 0.75 pu in the physical system. In order to preserve the per-unit value of power between the simulated and physical systems, the same scaling of 0.75 is applied to the physical current measurements before they are sent to the simulation. The arm voltage is 10% above the dc voltage 0.75 pu, i.e. 0.825 pu. The corresponding arm energy is the square of the arm voltage ($0.825^2 = 0.6805$ in pu). Figs. 13 and 14 show the rotor angles and speeds of G5 and G6 from the PHIL tests. The same pattern as the results from Section 6.2 is observed, where the POD causes the oscillations to propagate to AC Grid 1 and the energy support reduces the propagation by more than a factor of 3. Active power injected by Conv2P due to the POD action is shown in Fig. 15, which shows a significant amount of distortion due to noise. The noise is not reflected in the rotor angles and speeds because the ac system has large inertia which filters fast variations. Arm energy of the Conv2P is shown in Fig. 15 for the three cases. The findings are once again similar to the simulation cases. From Fig. 15, it can be seen the maximum variation in active power is $\simeq 0.005$ pu and the resulting variation in energy is $\simeq 0.02$ pu, which is inline with (11).

The experimental results show the same general trend as the simulation cases. However, when closely inspecting Figs. 9 and 13, it can be noted that the damping of the inter-area mode (Mode 2) is lower in the experimental case. This is mainly due to the time delays in the PHIL setup, i.e. the time elapsed from the measurement of the currents (or voltages) to the time when they are applied in the simulation (or power amplifier). These delays are caused mainly by the bandwidth of the power amplifier and one step time delays introduced to avoid algebraic loops in the simulation. In order to confirm the source of the mismatch between the simulation and PHIL results, the simulation was repeated taking into account the PHIL delays. Fig. 16 shows that there is a very good match between the simulation and the PHIL results when the time delays are considered (Sim + Delay).

8 Discussion

The results presented in the previous sections showed that AC Grid 2 in the system under test has a poorly damped (2.46%) electromechanical mode which was excited when a fault was applied to the system. The damping was then improved to 6.76% when POD was enabled on Conv2, the converter interfacing to AC Grid 2. However, this resulted in the oscillation of G6 (see Fig. 9),

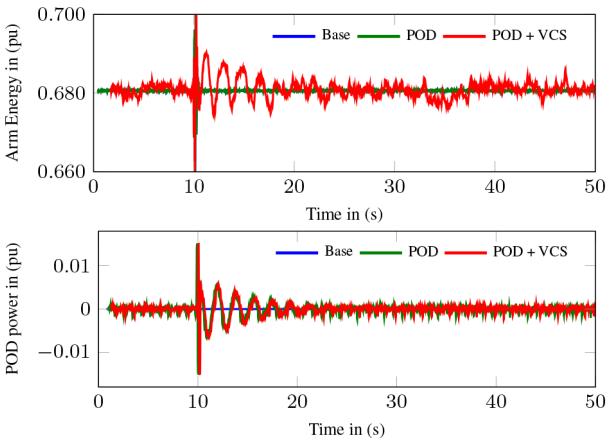

Fig. 15 *Active power and energy measurements of Conv2 (experimental)*

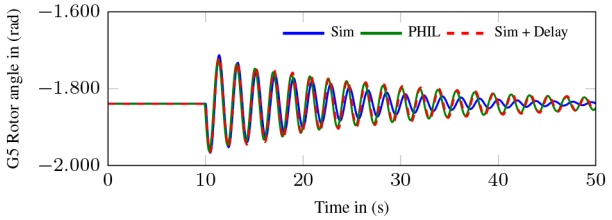

Fig. 16 *Comparison of simulation and experimental results*

a generator in AC Grid 1. Later, this effect was reduced by using the VCS method. The same effect was observed from the experimental results.

The amount of energy storage required for such a service can be calculated as shown in (11). Equation (11) can be used in two ways. The first method is to define the maximum active power required by the POD service and then use this value to calculate the extra energy required. The second approach is to define the maximum possible energy deviation and then specify the available POD power. The first approach is more challenging because the POD power can vary depending on a number of factors such as damping of the mode, magnitude and location of the disturbance, and inertia in the system. In this paper, the maximum energy deviation is specified to be 20% (10% maximum voltage deviation), which gives about 75 MW peak power [25 MW from each converter according to (11)]. This extra energy is obtained by either adding a few sub-modules or by increasing the operating voltage of each of the sub-modules. Increasing the sub-module capacitance reduces the voltage (energy) deviation for given peak power, which means that there will be fewer modules required or the voltage increase can be lowered. This action can be combined with the other two to obtain an optimal solution for a given application.

9 Conclusion

This paper explores the energy storage capability of the MMC to reduce the propagation of active power oscillations into connected ac grids due to the action of a POD controller.

The paper presents a detailed analysis and validation of a scheme to provide VCS to a dc grid. Since the virtual capacitance can be designed to be significantly larger than the equivalent dc grid capacitance, it provides a low impedance path for oscillating dc current. This action diverts the oscillations into the arm capacitors of the MMC instead of propagating them to the other ac grids.

A 21 bus system is used to investigate the effectiveness of the scheme using modal analysis, time-domain simulation, and PHIL tests. There is a strong correlation between the results from the three studies, and they all show that the scheme can effectively divert the oscillation into the arm capacitors. It was shown that the VCS method affects only the observability of the mode in other grids, not the damping or frequency, as expected. Additionally, the PHIL tests show that the scheme is practically applicable since it was implemented using a scaled MMC prototype.

A requirement for the scheme is that the converter is designed with a slightly higher storage capacity compared to nominal design, for example 10% increase in sub-module voltage was used in this study. The amount of additional capacity can be chosen depending on the desired level of participation of the converters in providing the service. Optimisation of such extra energy storage requirement can be taken as future work.

10 References

[1] 'Commission Regulation (EU) 2016/1447 of 26 August 2016 establishing a network code on requirements for grid connection of high voltage direct current systems and direct current-connected power park modules (Text with EEA relevance)', 2016

[2] Preece, R., Milanović, J.V.: 'Power oscillation damping using VSC-based multi-terminal HVDC grids', *IFAC Proc.*, 2012, **45**, (21), pp. 20–25

[3] Ndreko, M., van der Meer, A., Gibescu, M., *et al.*: 'Damping power system oscillations by VSC-based HVDC networks: a North Sea grid case study'. 12th Int. Workshop on Large-Scale Integration of Wind Power into Power Systems as Well as on Transmission Networks for Offshore Wind Power Plants, London, 2013

[4] Harnefors, L., Johansson, N., Zhang, L., *et al.*: 'Interarea oscillation damping using active-power modulation of multiterminal HVDC transmissions', *IEEE Trans. Power Syst.*, 2014, **29**, (5), pp. 2529–2538

[5] Trinh, N.T., Erlich, I., Teeuwsen, S.P.: 'Methods for utilization of MMC-VSC- HVDC for power oscillation damping'. 2014 IEEE PES General Meeting | Conf. Exposition, National Harbor, MD, USA, 2014, pp. 1–5

[6] Zeni, L., Eriksson, R., Goumalatsos, S., *et al.*: 'Power oscillation damping from VSC HVDC connected offshore wind power plants', *IEEE Trans. Power Deliv.*, 2016, **31**, (2), pp. 829–838

[7] Hertem, D.V., Gomis-Bellmunt, O., Liang, J.: 'Power system oscillation damping by means of VSC-HVDC systems', in: '*HVDC grids: for offshore and supergrid of the future*' (Wiley-IEEE Press, Chichester, West Sussex, UK, 2016), pp. 391–411

[8] Kundur, P., Balu, N.J., Lauby, M.G.: '*Power system stability and control*' (McGraw-Hill, New York, 1994), oCLC: 28929603

[9] Endegnanew, A.G., Kalemba, L., Uhlen, K.: 'Using decentralized control techniques for interaction analysis in hybrid AC/DC grids'. 2018 IEEE Power Energy Society General Meeting (PESGM), Portland, OR, USA, 2018, pp. 1–5

[10] Barker, C.D., Whitehouse, R.S., Adamczyk, A.G., *et al.*: 'Low frequency active power oscillation damping using a MMC-VSC HVDC link'. 13th IET Int. Conf. on AC and DC Power Transmission (ACDC 2017), Manchester, UK, 2017, pp. 1–6

[11] Taffese, A.A., Tedeschi, E., de Jong, E.: 'A control scheme for utilizing energy storage of the modular multilevel converter for power oscillation damping'. 2017 IEEE 18th Workshop on Control and Modeling for Power Electronics (COMPEL), Stanford, CA, USA, 2017, pp. 1–8

[12] Taffese, A.A., Tedeschi, E.: 'Coordination of modular multilevel converter based HVDC terminals for ancillary services'. 2018 Power Systems Computation Conf. (PSCC), Dublin, Ireland, 2018, pp. 1–7

[13] Wang, X., Du, W.: 'Virtual inertia control of grid-connected wind farms'. Int. Conf. on Renewable Power Generation (RPG 2015), Beijing, China, 2015, pp. 1–6

[14] Freytes, J., Rault, P., Gruson, F., *et al.*: 'Dynamic impact of MMC controllers on DC voltage droop controlled MTDC grids'. 2016 18th European Conf. on Power Electronics and Applications (EPE'16 ECCE Europe), Karlsruhe, Germany, 2016, pp. 1–10

[15] Freytes, J., Akkari, S., Rault, P., *et al.*: 'Dynamic analysis of MMC-based MTDC grids: use of MMC energy to improve voltage behavior', *IEEE Trans. Power Deliv.*, 2019, **34**, (1), pp. 137–148

[16] Shinoda, K., Benchaib, A., Dai, J., *et al.*: 'Virtual capacitor control: mitigation of DC voltage fluctuations in MMC-based HVdc systems', *IEEE Trans. Power Deliv.*, 2018, **33**, (1), pp. 455–465

[17] Brandl, R., Calin, M., Degner, T.: 'Power hardware-in-the-loop setup for power system stability analyses', *CIRED – Open Access Proc. J.*, 2017, **2017**, (1), pp. 387–390

[18] Luo, K., Shi, W., Tang, H.: 'Implementation and value of power hardware in the loop testing bed for wind turbines integrated into grid', *J. Eng.*, 2017, **2017**, (13), pp. 1635–1639

[19] Bergna-Diaz, G., Suul, J.A., D'Arco, S.: 'Energy-based state-space representation of modular multilevel converters with a constant equilibrium point in steady-state operation', *IEEE Trans. Power Electron.*, 2017, **PP**, (99), pp. 1–19

[20] Debnath, S., Qin, J., Bahrani, B., *et al.*: 'Operation, control, and applications of the modular multilevel converter: a review', *IEEE Trans. Power Electron.*, 2015, **30**, (1), pp. 37–53

[21] Bergna Diaz, G., Suul, J.A., D'Arco, S.: 'Small-signal state-space modeling of modular multilevel converters for system stability analysis'. 2015 IEEE Energy Conversion Congress and Exposition (ECCE), Montreal, QC, Canada, 2015, pp. 5822–5829

[22] Mohan, N., Undeland, T.M.: '*Power electronics: converters, applications, and design*' (John Wiley & Sons, New Jersey, USA, 2007)

[23] 'Simscape Documentation'. Available at https://se.mathworks.com/help/physmod/simscape/, accessed 4 May 2019

[24] Gonzalez-Longatt, F., Rueda, J.L. (eds.): *'Powerfactory applications for power system analysis', Power systems* (Springer International Publishing, Basel, Switzerland, 2014)
[25] Leterme, W., Ahmed, N., Beerten, J., *et al.*: 'A new HVDC grid test system for HVDC grid dynamics and protection studies in EMT-type software'. 11th IET Int. Conf. on AC and DC Power Transmission, Birmingham, UK, 2015, pp. 1–7
[26] Domínguez-García, J.L., Ugalde-Loo, C.E., Bianchi, F., *et al.*: 'Input–output signal selection for damping of power system oscillations using wind power plants', *Int. J. Electr. Power Energy Syst.*, 2014, **58**, pp. 75–84
[27] Chow, J.H., Boukarim, G.E., Murdoch, A.: 'Power system stabilizers as undergraduate control design projects', *IEEE Trans. Power Syst.*, 2004, **19**, (1), pp. 144–151
[28] Endegnanew, A.G.: 'Stability analysis of high voltage hybrid AC/DC power systems'. PhD Dissertation, Trondheim, Norway, 2017
[29] 'Real-Time simulation'. Available at https://www.opal-rt.com/, accessed 4 May 2019
[30] 'EGSTON POWER'. Available at https://www.egstonpower.com/, accessed 4 May 2019
[31] D'Arco, S., Endegnanew, A.G., Guidi, G., *et al.*: 'Interoperability of modular multilevel converters and 2-level voltage source converters in a laboratory-scale multi-terminal DC grid'. 2018 Int. Power Electronics Conf. (IPEC-Niigata 2018 -ECCE Asia), Niigata, Japan, 2018, pp. 2003–2010
[32] Ren, W., Steurer, M., Baldwin, T.L.: 'Improve the stability and the accuracy of power hardware-in-the-loop simulation by selecting appropriate interface algorithms'. 2007 IEEE/IAS Industrial Commercial Power Systems Technical Conf., Edmonton, Alta., Canada, 2007, pp. 1–7

11 Appendix

11.1 Per-unit base values

The base values used for per-unit calculations for the converters are depicted in (13). The base for both simulated and physical converters is given in the next section:

$$
\begin{aligned}
&I_{\mathrm{b}}^{\mathrm{ac}} = \frac{2}{3}\frac{S_{\mathrm{b}}}{V_{\mathrm{b}}^{\mathrm{ac}}}, \quad Z_{\mathrm{b}}^{\mathrm{ac}} = \frac{V_{\mathrm{b}}^{\mathrm{ac}}}{I_{\mathrm{b}}^{\mathrm{ac}}}, \quad I_{\mathrm{b}}^{\mathrm{dc}} = \frac{S_{\mathrm{b}}}{V_{\mathrm{b}}^{\mathrm{dc}}}, \quad Z_{\mathrm{b}}^{\mathrm{dc}} = \frac{V_{\mathrm{b}}^{\mathrm{dc}}}{I_{\mathrm{b}}^{\mathrm{dc}}} \\
&L_{\mathrm{b}}^{\mathrm{ac}} = Z_{\mathrm{b}}^{\mathrm{ac}}, \quad C_{\mathrm{b}}^{\mathrm{ac}} = \frac{1}{Z_{\mathrm{b}}^{\mathrm{ac}}}, \quad L_{\mathrm{b}}^{\mathrm{dc}} = Z_{\mathrm{b}}^{\mathrm{dc}}, \quad C_{\mathrm{b}}^{\mathrm{dc}} = \frac{1}{Z_{\mathrm{b}}^{\mathrm{dc}}} \\
&V_{\mathrm{b}}^{\mathrm{ac}} = \frac{1}{2}V_{\mathrm{b}}^{\mathrm{dc}}, \quad W_{\mathrm{b}} = \frac{1}{2}C_{\mathrm{arm}}\left(V_{\mathrm{b}}^{\mathrm{dc}}\right)^2
\end{aligned} \tag{13}
$$

11.2 Converter and DC cable parameters

Parameters for the simulated and physical converters are shown in Tables 5 and 6, respectively. The dc cables are rated for 900 MW at ± 320 kV (total voltage 640 kV). They are represented by a π-equivalent model with resistance per km of 0.0001 pu and shunt capacitance per km of 0.02 μF. The converter controllers are implemented as presented in [11, 12]. The MMC variables are grouped into ac and dc sides for per-unit conversion. The ac side includes ac currents and voltages. The remaining variables, such as arm voltages and currents, are considered as dc.

11.3 Synchronous machine parameters

The generators in this paper are represented by a detailed sixth-order model [8] with parameters shown in Table 7. All generators are rated for 900 MW and have the same parameters except inertia time constant, H. The value of H is 6 s for G1, G2, and G3, while G4, G5, and G6 have 6.75 s. The automatic voltage regulator used with all the generators is of the simplified excitation system type. Hydro governor, HYGOV1, is used for G2, G3, and G5. The rest of the generators are gas turbine type (TGOV1). The transmission lines are represented by π-equivalent model with the $r = 0.0001$ pu/km and $x = 0.001$ pu/km with power and voltage rating of 100 MW and 380 kV, respectively. The transformers are rated for 900 MW and have per-unit impedance of $0 + 0.15$i.

Table 5 HVDC converter parameters [25]

Parameter	Value
base apparent power, S_{b}	900 MVA
base dc voltage, $V_{\mathrm{b}}^{\mathrm{dc}}$	640 kV
frequency, ω	$2\pi 50$ rad/s
arm capacitance, $C_{\mathrm{arm}} = C_{\mathrm{SM}}/N$	29 μF
arm inductance, L_{arm}	84 mH
arm resistance, R_{arm}	0.885 Ω
transformer reactance, X_{t}	17.7 Ω
transformer resistance, R_{t}	1.77 Ω

Table 6 Scaled prototype converter parameters

Parameter	Value
base apparent power, S_{b}	60 kVA
base dc voltage, $V_{\mathrm{b}}^{\mathrm{dc}}$	600 V
frequency, ω	$2\pi 50$ rad/s
arm capacitance, $C_{\mathrm{arm}} = C_{\mathrm{SM}}/N$	1250 μF
arm inductance, L_{arm}	1.4 mH
arm resistance, R_{arm}	0.1 Ω
transformer reactance, X_{t}	0.22 Ω
transformer resistance, R_{t}	0.01 Ω

Table 7 Generator parameters [8]

Parameter	Value	Parameter	Value	Parameter	Value
X_d	1.8	X_q	1.7	X_l	0.2
X'_d	0.3	X'_q	0.55	X''_d	0.25
X''_q	0.25	R_a	0.0025	T'_{d0}	8 s
T'_{q0}	0.4 s	T''_{d0}	0.03 s	T''_{q0}	0.05 s